Computational Modelling of Ceria-Based Solid Oxide Fuel Cell Electrolyte Materials

Ahmed, Mohamed; Rodley, David; Jones, Thomas; Abdolvand, Amin; Lightfoot, Alison; Fruchtl, Herbert

Published in:
ECS Transactions

DOI:
10.1149/10301.0931ecst

Publication date:
2021

Document Version
Peer reviewed version

Computational Modelling of Ceria-Based Solid Oxide Fuel Cell Electrolyte Materials

Mohamed Ahmed [a,b], David Rodley [a], Thomas D. A. Jones [a], Amin Abdolvand [a], Alison E. Lightfoot [b], Herbert Früchtl [b], Richard T. Baker [b]

[a] School of Science and Engineering, University of Dundee, Dundee, DD1 4HN, UK
[b] EaStCHEM School of Chemistry, University of St Andrews, St Andrews, KY16 9ST, UK

A simulation methodology for calculating the lattice parameter and oxygen ion migration energy of ceria-based electrolyte formulations is devised. The results are analysed and benchmarked against experimentally obtained values to verify the efficacy of the simulation methodology. A total of 26, 2 x 2 x 2 samarium (Sm)- and gadolinium (Gd)-doped supercells of different compositions and doping profiles were modelled and simulated by molecular mechanics force field methods using CP2K. The results of the computational simulations are comparable with those obtained experimentally, especially when there are equal amounts of Sm and Gd dopants in the structure. Simulation results can also provide insights into the mechanisms of ionic conduction. The incongruence of the computational and experimental results is attributed to the limitations of the molecular mechanics force field methodology utilised, with the expectation that an ab initio density functional theory (DFT) calculation would yield closer conformance.

Introduction

Recent significant advances in materials development for solid oxide fuel cells (SOFCs), and modelling techniques have challenged researchers to develop streamlined methodologies aiming at faster and more reliable fabrication of highly efficient cells. Instead of adopting a trial-and-error technique to discover the optimal composition of fuel cell component materials, computational techniques can predict the most appropriate compositions in a cost-effective and timely manner. Over the years many formulations of SOFC electrolytes have been studied.

A seminal first-principles study of the ionic conductivity in doped ceria indicated that multiple doping with different trivalent cations would yield higher ionic conductivity than that which would be obtained with single-species doping (1). The theory that the interaction between the dopant cations and the oxygen vacancies results in the relaxation of interatomic distances (1), and the subsequent postulate that the critical dopant ionic radius is a necessary but insufficient condition for enhanced ionic conductivity (2,3), led to further research to investigate the effect of co-doping on the ionic conductivity and the geometry of the cell.

Baker and Coles-Aldridge (4) produced singly-, doubly-, and triply-doped ceria crystals using Sm, Gd, and neodymium (Nd) as dopants. The concentrations of the individual dopants were varied but the total dopant concentration was fixed. It was concluded that co-doping with Sm and Gd resulted in the lowest activation energy and the highest conductivity in the intermediate temperature range (300 – 700 ℃) (4). Further work by Baker and Coles-Aldridge (5) studied two compositional series of co-doped ceria: the first series had equal amounts of Sm and Gd in each structure and variable total dopant concentration, and the second series had a fixed total dopant concentration in each structure but with variable amounts of Sm and Gd. Their study concluded that equal amounts of Sm and Gd dopants yielded higher conductivities at temperatures greater than or equal 500 ℃.

The current study aims to perform an atomic-level computational simulation of a co-doped SOFC electrolyte by modelling the Sm- and Gd-doped compositions used in (5), to calculate the lattice parameter and the activation (or migration) energy. The results are analysed and benchmarked against the results obtained experimentally in (5). Moreover, the study aims at showing the importance of simulation as a research tool that may complement or precede experiment. It precedes experiment when testing many chemical compositions is required without conducting the actual synthesis and lab testing of each composition, thereby introducing considerable time and cost savings into the research lifecycle. It complements experiment when a theory is needed to explain an observation by generating simulations of events that can occur in the femtosecond or smaller time scales.

The Compositional Series

In the current study, a 2 x 2 x 2 pure ceria supercell consisting of 32 cerium atoms and 64 oxygen atoms was taken as the base undoped structure. Such a supercell would consist of 8 ceria unit cells (or minicubes). In line with (5), two compositional series of doped ceria were modelled.

Series 1. The first series has equal amounts of samarium and gadolinium in each structure, resulting in a series of structures of different total dopant concentration. The amount of dopants is taken as the number of atoms that substitute the cerium atoms in the supercell. Naturally, a maximum of 32 dopant atoms were allowed in the structures of this series. The modelled structures were Sr1S0G0 (undoped structure), Sr1S1G1, Sr1S2G2, Sr1S8G8, and Sr1S16G16 where S and G denote samarium and gadolinium respectively, and the number after the symbol specifies the number atoms for the kind represented by the symbol. The last structure (Sr1S16G16) is a hypothetical structure where all Ce atoms are assumed to have been substituted by the dopant atoms which will now interact with the pure ceria oxygen sublattice.

Series 2. The second series has equal total dopant concentration across all the structures in the series but with different amounts of samarium and gadolinium in each structure. The total number of dopant atoms was fixed at eight. Thus, the modelled structures were Sr2S0G8, Sr2S1G7, Sr2S2G6, Sr2S3G5, Sr2S4G4, Sr2S5G3, Sr2S6G2, Sr2S7G1, and Sr2S8G0. Sr2S4G4 may also belong to the first series, but it was decided to keep it as a member of the second series.

The addition of two dopant atoms to the pure ceria crystal results in the formation of one oxygen vacancy as shown for samarium in Equation (1) written in the Kröger-Vink notation for crystal defects (6):

$$Sm_2O_3 \rightarrow 2Sm'_{Ce} + 3O_O^{\times} + v_O^{\cdot\cdot} \quad [1]$$

Therefore, each dopant atom will substitute one cerium atom, and for every two dopant atoms one oxygen vacancy will be formed. The structures modelled in the current study will therefore have the general formula shown below.

$$Ce_{32-(x+y)}Sm_xGd_yO_{64-\frac{x+y}{2}} \quad [2]$$

Table I shows the structure of each member in the two compositional series and its notation.

TABLE I. The Compositional Series.

Structure	Notation
Series 1	
$Ce_{32}O_{64}$	Sr1S0G0
$Ce_{30}Sm_1Gd_1O_{63}$	Sr1S1G1
$Ce_{28}Sm_2Gd_2O_{62}$	Sr1S2G2
$Ce_{16}Sm_8Gd_8O_{56}$	Sr1S8G8
$Sm_{16}Gd_{16}O_{48}$	Sr1S16G16
Series 2	
$Ce_{24}Gd_8O_{60}$	Sr2S0G8
$Ce_{24}Sm_1Gd_7O_{60}$	Sr2S1G7
$Ce_{24}Sm_2Gd_6O_{60}$	Sr2S2G6
$Ce_{24}Sm_3Gd_5O_{60}$	Sr2S3G5
$Ce_{24}Sm_4Gd_4O_{60}$	Sr2S4G4
$Ce_{24}Sm_5Gd_3O_{60}$	Sr2S5G3
$Ce_{24}Sm_6Gd_2O_{60}$	Sr2S6G2
$Ce_{24}Sm_7Gd_1O_{60}$	Sr2S7G1
$Ce_{24}Sm_8O_{60}$	Sr2S8G0

Doping Strategies Employed

During the chemical synthesis of doped ceria crystals, dopants replace cerium atoms in random positions within the crystal. However, a remarkable feature of modelling doped crystal structures is the possibility of controlling the positions of dopants and oxygen vacancies. To exploit this computational advantage, two doping strategies (DSα and DSβ) were devised in order to study the effect of varying the doping profile of the crystal on its geometry and activation energy. Each doping strategy was applied in both compositional series. Both doping strategies reflect homogeneous doping by substituting cerium in

symmetrical positions with samarium or gadolinium, and removing oxygen atoms to create oxygen vacancies in the nearest neighbour positions to the cation dopants (1).

DSα. The first doping strategy places one dopant atom in two or more of the eight minicubes of the 2 x 2 x 2 supercell for Series 1 structures except for the Sr1S8G8 structure, where two dopant atoms of different kinds are placed in each minicube. The positions of the dopants are chosen to be symmetrically equivalent. For Series 2, DSα places one dopant atom in each minicube starting with one gadolinium atom in each minicube for the Sr2S0G8, and then progressively replacing one gadolinium atom with one samarium atom in each of the subsequent structures of this series until there is one samarium atom in each minicube for the Sr2S8G0 structure. In all cases, the removed oxygen atoms are chosen to be the nearest neighbour to the dopant atom(s).

DSβ. The second doping strategy, denoted DSβ, places the dopants exclusively in four diametrical minicubes, allowing the dopants to be as far as possible from each other. However, for structure Sr1S1G1, the dopants are placed in the same minicube to differentiate it from the same structure in the first doping strategy DSα.

Computational Methodology

Software

The computations were carried out using CP2K (a free and open-source program available from www.cp2k.org) version 7.0. CP2K is a computational chemistry and solid-state physics software package that can perform simulations on the atomic level (7). Cryst (8) is a software package which can convert between various file formats of crystals in addition to creating neighbour lists for specific elements in a crystal that are within user – specified distances. It also introduces dopants and vacancies at various lattice positions and creates input files to carry out nudged elastic band (NEB) calculations for CP2K and other computational chemistry packages.

The crystal structure of the cerium dioxide unit cell utilized in this study was obtained from the Crystallography Open Database (COD) in the Crystallographic Information File (.cif) format (Filename: 4343161.cif). This experimentally obtained structure shows that the cell is cubic and belongs to the $Fm\bar{3}m$ space group, and has a 5.40972 Å cell parameter (9). As the unit cell of cerium dioxide has four formula units of CeO_2, the 2x2x2 supercell consists of 32 cerium atoms and 64 oxygen atoms.

Cell Optimization

Cell optimization is an iterative computational procedure where initial values for the lattice parameter and the atomic coordinates serve as inputs. After the optimization procedure has converged, the optimized lattice parameter and atomic coordinates are output to a file. The initial values for the pure ceria crystal are taken from the .cif file. Cell optimization is then carried out on the pure ceria crystal. Doped structures are obtained by replacing cerium atoms with dopant atoms and removing oxygen atoms from the optimized pure ceria crystal.

The components of the long-range potential were modelled using the soft particle mesh Ewald (SPME) sums method and 3D Fast Fourier Transforms (FFT) (10,11). A fixed cut-off is used to compute the direct sum, and a Cardinal B-spline interpolation followed by Euler exponential spline interpolation to get smooth approximations of the energies, forces, and positions (10).

Owing to the high polarizability of the oxide ion, the short-range potential components are modelled using the DIPole Polarizable Ion Model (DIPPIM) (12), which consists of overlap repulsive interactions between electrons, damped dispersion attractive van der Waals interactions, and polarization interactions (13–15). The polarization interactions are calculated using Born – Mayer – Huggins – Fumi – Tosi Damped (BMHFTD) potential in terms of the Tang – Toennies dispersion damping function (13,14,16,17).

The geometry and cell optimization were carried out using the conjugate gradient method, which carries out line search in directions that obey the orthogonality condition for the Hessian matrix of the preceding step and the take account of the current negative gradient and the previous search direction (18). CP2K uses a combination of golden section search and Brent's methods (19) to accelerate the convergence towards the minimum point.

The KEEP_SYMMETRY keyword in the &CELL_OPT section in the CP2K input files was set to TRUE and the SYMMETRY keyword in the &CELL section was set to CUBIC in order to preserve the geometry of the resulting optimized supercell in the cubic form in order to simulate the experimental results obtained by X-Ray Diffraction (XRD) of pure and doped ceria powder and pellets showing that the crystals retain their cubic $Fm\bar{3}m$ structures after synthesis (4,5).

CP2K was instructed to generate neighbour lists in the &NEIGHBOR_LISTS section of the input file in order to show the distances between all the atoms in the supercell in order to select the proper positions of the vacancies relative to the positions of the dopant atoms when building up the doping profile. The positions of the symmetrically equivalent atoms were determined using SPGLIB (20) which is a library to find crystal symmetries written in C (https://atztogo.github.io/spglib/). The library function spg_get_symmetry_with_collinear_spin was used to get the symmetrically equivalent positions.

Cell optimization for the doped ceria for each of the structures in the two compositional series devised for this study and for each doping strategy was performed to obtain the lattice parameter of each structure. The positions of the dopant atoms and oxygen vacancies are specified in the &CELL subsection of the input file. The dopant atoms substitute cerium atoms, and the oxygen vacancies are created by deleting the corresponding oxygen atoms from the crystal structure.

Activation Energy

To estimate the activation energies associated with hopping of an oxygen ion from a specific site to a neighbouring site in the structures studied, the following steps were applied:

1. The positions of the dopant atoms in the pure crystal were assigned.
2. The neighbour list of all oxygen atoms at a distance within 3.0 Å was generated.

3. The climbing image nudged elastic band (CI-NEB) method was applied to determine all activation barriers for a nearest-neighbour oxygen moving to a vacancy position in the doped crystal.
4. The average energy barrier was calculated.

The nudged elastic band is a method of the harmonic transition state theory used for finding the minimum energy path (MEP) between two conformations of a crystal (21,22). In this work, it was used to describe an oxide ion hopping from an initial position into a final position in an oxygen vacancy.

Each crystal structure was scanned for all energy barriers (or saddle points) to the migration of each oxygen atom to its neighbouring oxygen vacancy, generated in the 'neighbour_list' file (created by the cryst program as described above), to estimate the activation energy. This was done utilizing a bash script looping over all possible initial and final positions. The script reads the positions of each two neighbouring oxygen atoms in the 'neighbour_list' file and creates a CP2K input file to run a nudged elastic band (NEB) computation to find the energy barrier to the migration of one of the oxygen atoms to the vacant position of the other. The results of the computation, namely the energies at the initial, saddle, and final positions are added to the 'barriers.dat' file. Due to the simple nature of the barrier and the "climbing image" method used to locate the energy maximum of the transition, it was sufficient to specify three replicas in each NEB calculation. The end points of the elastic band were also optimized using the geometric DIIS (Direct Inversion in the Iterative Space) method (18), as requested through the OPTIMIZE_END_POINTS keyword.

The average energy barrier of each structure is calculated from the formula (18):

$$\langle E_b \rangle = -kT\ ln\left(\frac{1}{M}\sum_{i=1}^{M} e^{-\frac{\Delta E_i^{SE}}{kT}}\right) \quad [3]$$

where ΔE_i^{SE} is the difference between the saddle point energy and the band initial and final energies for the oxygen neighbour pair i, and M is the number of energy barriers; in this study $M = 384$ and $T = 500℃$. As the migration enthalpy dominates at temperatures of 500℃ or higher (1,5), a temperature of 500℃ was selected in this study for the calculation of the Boltzmann factor and the partition function.

Statistical Analysis

Tests for statistical significance of the difference between the means of two samples were carried out using 2-sample Student's *t*-test for the mean with the condition of statistical significance taken as $p < .05$. The calculations were done using Minitab® 20.

Results and Discussion

Lattice Parameter

It was specified to CP2K that the cell geometry shall be kept cubic during the cell optimization run. Thus, the lengths of the three resulting cell vectors for each structure shall be equal, and the lattice parameter can be calculated from any one of them. CP2K shows the output cell vectors in the &CELL section of the '{Project_Name}-1.restart' file. Since a 2 x 2 x 2 supercell was modelled, the lattice parameter is equal to half the value of the cell vector.

Figures 1 – 4 compare the trends in the variation of the lattice parameter as a function of the samarium mole fraction in the computational results obtained in this work and the experimental results obtained in (5). When constructing these figures, the experimental data was assumed to be identical for both DSα and DSβ doping strategies. As with the experimental plots, the computational plots show the strong linear dependence of the lattice parameter on the dopant concentration according to Vegard's law (4,5,9,23,24).

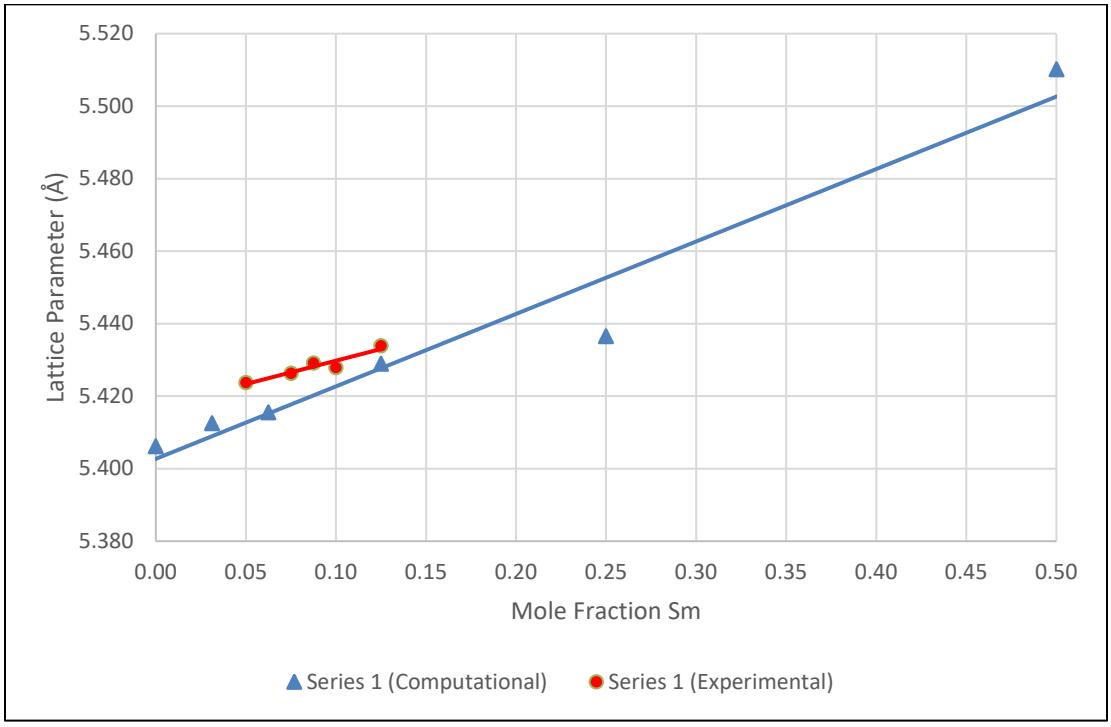

Figure 1. Comparison of the computational and experimental variation of the lattice parameter with Sm mole fraction for compositional Series 1 and doping strategy DSα.

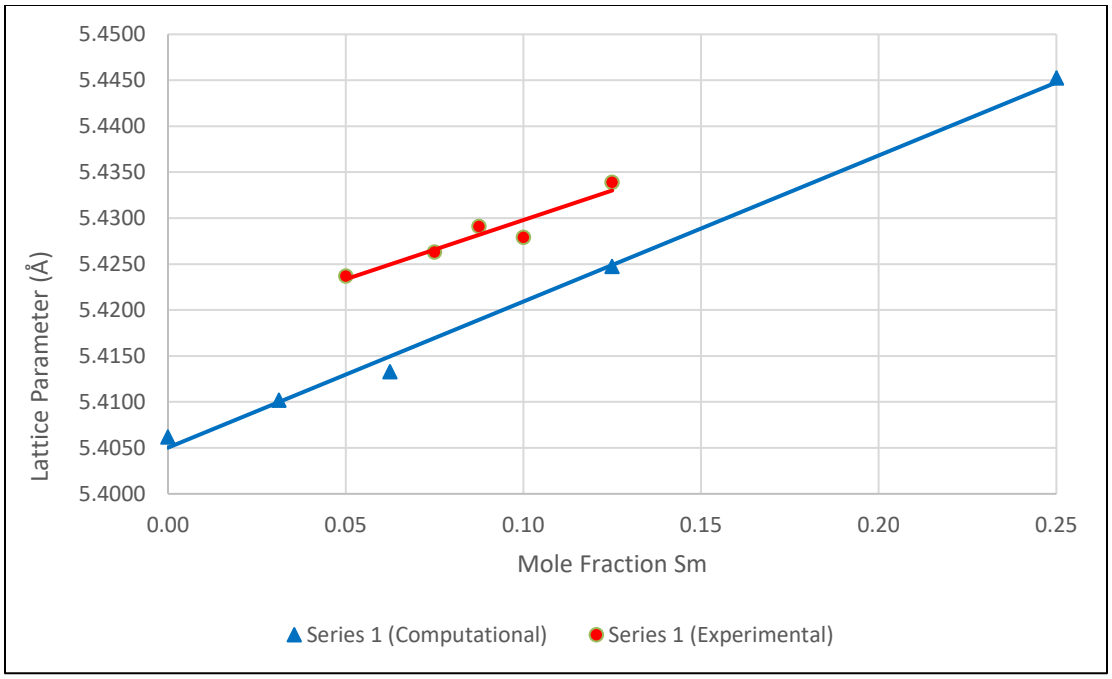

Figure 2. Comparison of the computational and experimental variation of the lattice parameter with Sm mole fraction for compositional Series 1 and doping strategy DSβ.

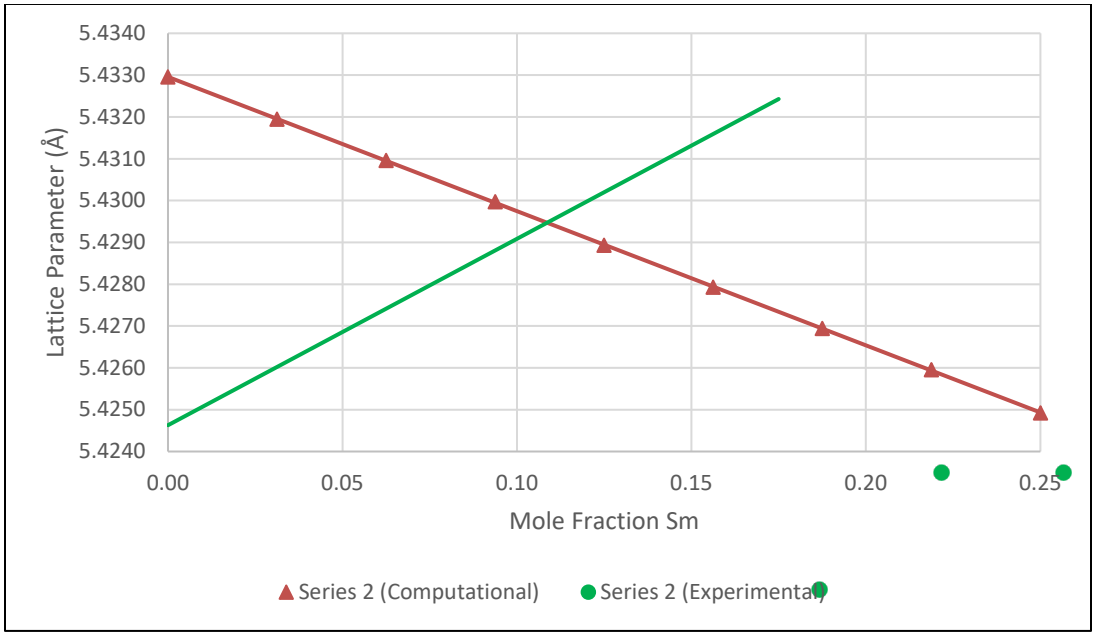

Figure 3. Comparison of the computational and experimental variation of the lattice parameter with Sm mole fraction for compositional Series 2 and doping strategy DSα.

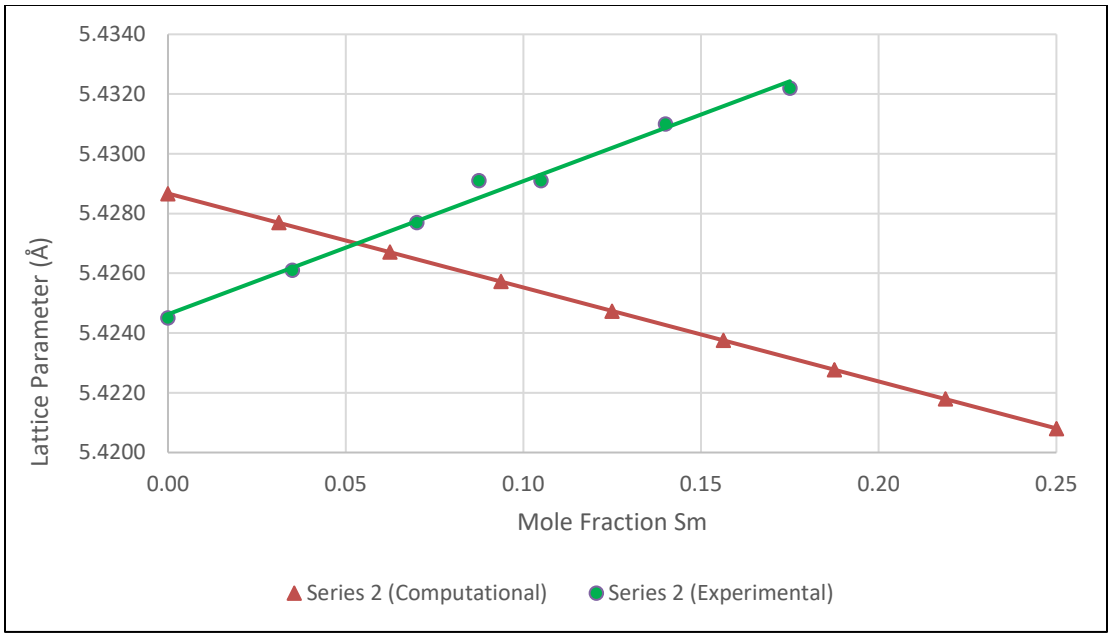

Figure 4. Comparison of the computational and experimental variation of the lattice parameter with Sm mole fraction for compositional Series 2 and doping strategy DSβ.

Specific to the computational plots, it can be noted that both doping strategies result in a similar trend within each compositional series, i.e., DSα and DSβ exhibit the same trend in the lattice parameter results of Series 1 (Figures 1 and 2) when varying total dopant concentration, and they exhibit the same trend in the lattice parameter results of Series 2 (Figures 3 and 4). It was also found that the difference in the values of the Series 1 lattice parameter for DSα compared with those of DSβ was statistically nonsignificant ($p > .05$), while the difference in the values of the Series 2 lattice parameter was statistically significant ($p = .005$). This result indicates that if the total dopant concentration is kept constant while the amounts of individual dopants are not equal, then the kind, amount, and the position of each individual doping species, and, consequently, the position of the oxygen vacancies will all determine the lattice parameter of the doped crystal. On the other hand, if the individual doping species are added in equal amounts, their position within the crystal will not play a significant role in determining the lattice parameter of the crystal. The importance of making these inferences based on computational modelling cannot be overemphasized.

On comparing the lattice parameter results of the computational and experimental work, an evident feature in the results for Series 1 is that the domain of computational results is much wider than that of the experimental results; from 0 to 0.5 mol fraction Sm for DSα, and from 0 to 0.25 mol fraction Sm for DSβ versus from 0.05 to 0.13 mol fraction Sm for experimental results. This demonstrates the flexibility in carrying out more "experiments" computationally on the same system. Despite the obvious difference in the extents of the domains of the experimental and computational lattice parameter results of Series 1, the graphical trends are the same for both DSα and DSβ, and, more importantly, the differences between the computational and experimental values of the lattice parameter of Series 1 are statistically nonsignificant ($p > .05$) for both DSα and DSβ.

On the other hand, the evident feature in the results for the lattice parameter of Series 2 is that the graphical trends of the computational and experimental results are contradictory. However, it was found that the differences between the computational and experimental values of the lattice parameter of Series 2 are still statistically nonsignificant ($p > .05$) for DSα but significant ($p = .015$) for DSβ. These mixed results reflect the naturally random doping strategies of the compositions that are prepared experimentally in the laboratory; there is no equivalent for DSα and DSβ in the experimental benchmark. But the emergence of mixed results for the lattice parameters of Series 2 and not in Series 1 should be expected considering the theoretical postulate stated above, viz., the position of the dopants is the primary factor that determines the lattice parameter when the total dopant concentration is fixed (Series 2), while it has a negligible or no effect otherwise (Series 1). DSα, being less restrictive in the placing of dopants and vacancies inside the crystal than DSβ, is thus more representative of the random dopant and vacancy locations elicited in the laboratory and, therefore, shows nonsignificant difference in the lattice parameter from the experimental benchmark despite their apparently opposite graphical trends.

Still, the limitations of the computational methodology utilized in calculating the lattice parameter in this study cannot be overlooked. The cell optimization computation was carried out without taking the temperature, the bonding between the elements comprising the crystal, and the variation of the coordination number of the cations due to the variation in the position of the oxygen vacancies into consideration.

Activation Energy

Unique to the computational methodology is the ability to calculate the energy barriers (or saddle points) for each ionic hop, which cannot be obtained experimentally. The sets of all energy barriers for each of the studied 26 structures are given in 26 different 'barriers.dat' files. An excerpt from the contents of a 'barriers.dat' file is shown in Figure 5, where the first two numbers in each line are the positions of the oxide ion and the oxygen vacancy, and the third, fourth, and fifth numbers in each line are the initial, saddle, and final energy states of the hop, respectively, in Hartree (1 Hartree = 27.211 eV).

```
7 34 -115.096458767 -115.075526369 -115.097430565
7 57 -115.096434435 -115.065117942 -115.098534381
8 9 -115.096407793 -115.065890964 -115.096407730
8 10 -115.096434641 -115.082790905 -115.096434641
8 11 -115.096434651 -115.070052300 -115.097120168
8 23 -115.096434480 -115.078110839 -115.096978626
```

Figure 5. An excerpt from an exemplary 'barriers.dat' file showing the positions of the oxide ion and vacancy in addition to the initial, saddle, and final energy states.

Figures 6 and 7 show the energy profiles of DSα and DSβ structures, respectively. The introduction of a dopant into the pure crystal causes a decrease in the saddle point energy. The energy needed for an oxide ion to migrate into any vacancy in the undoped structure Sr1S0G0 is higher than that needed for doped structures. Moreover, for the undoped structure, the same amount of energy is needed for hopping into any neighboring vacancy. However, with increasing doping concentration the energy barriers are reduced, resulting in higher ionic conductivity.

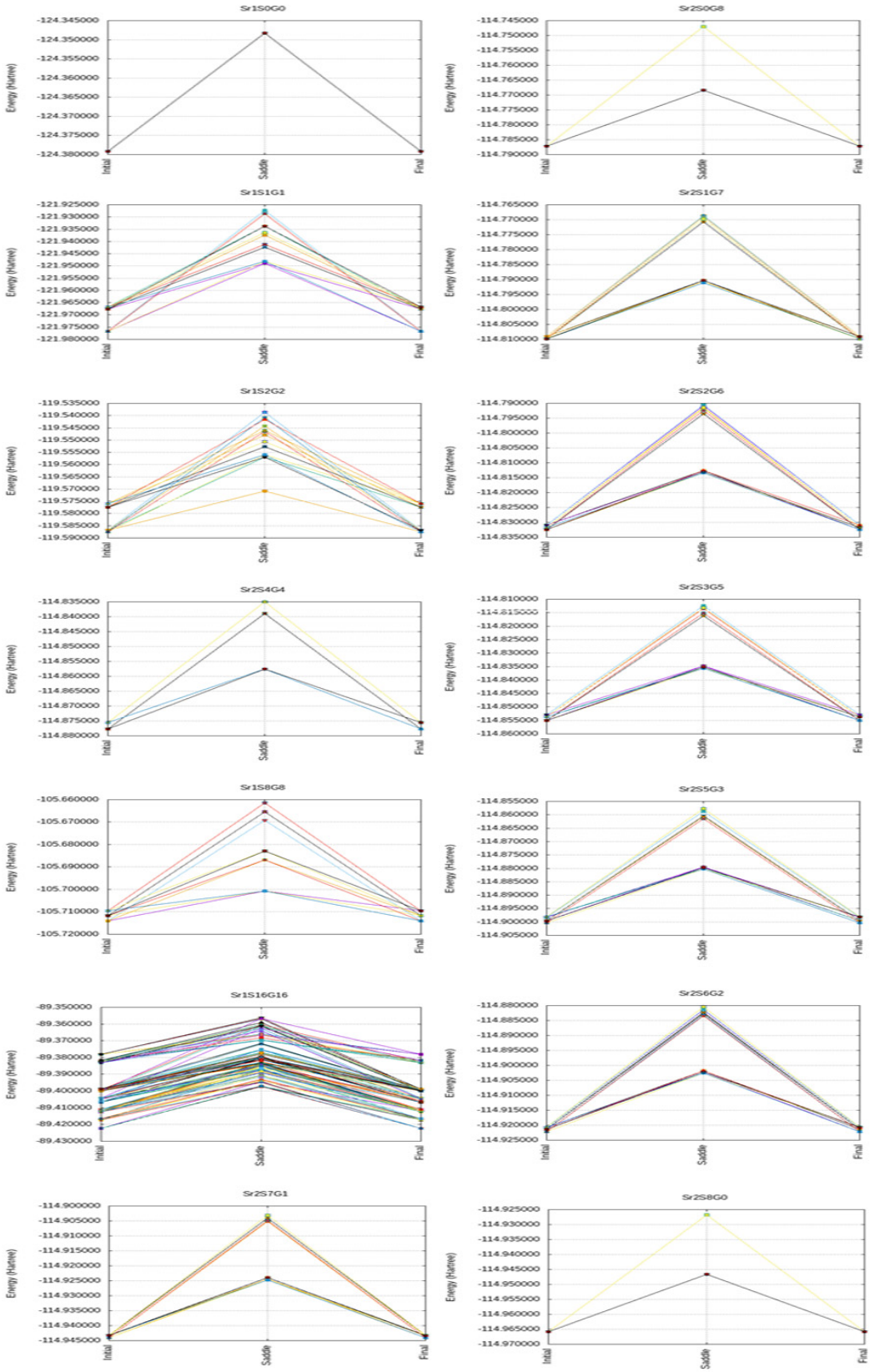

Figure 6. Energy profiles showing computed saddle points for all compositional series with doping strategy DSα.

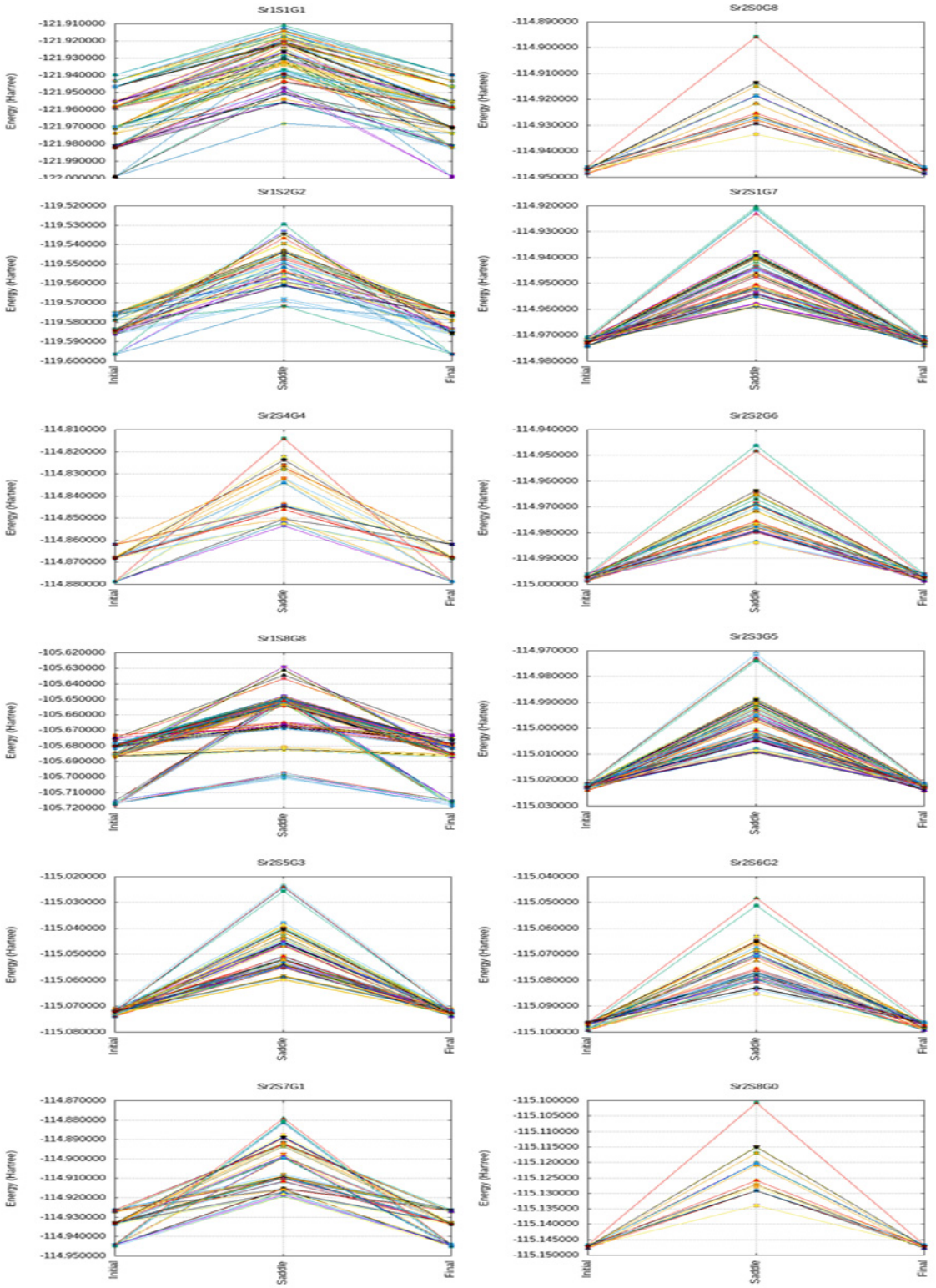

Figure 7. Energy profiles showing computed saddle points for all compositional series with doping strategy DSβ.

The two modelled doping strategies result in different distributions of the energy barriers within the crystal for the same structure. For example, comparing the lightly doped

structure Sr1S1G1 in DSα and DSβ doping strategies, the energy barriers are more graphically "dispersed" for DSβ than for DSα; the energy required for oxide ions to hop into vacancies is more variable in case the dopant separation distances are maximised (Figure 7) than when they are less restrictively distributed (Figure 6). Such remarkable variation in the energy profiles of the oxide ion hops within a single structure could introduce an error in the calculation of the activation energy. It is interesting to note that the hypothetical Sr1S16G16 structure where cerium atoms are fully substituted by the dopants (Figure 6) provide the lowest energy profile of all calculated structures.

The shapes of the energy profiles of Series 2 structures in Figures 6 and 7, where the total dopant concentration is fixed and the Sm:Gd ratio is varied, are remarkably similar. The increase in Sm causes the energy barriers to exhibit more variation, with such variation significantly more pronounced, again, in DSβ than in DSα. Also, for DSβ (Figure 7), the dispersion starts to decrease with Sm:Gd is at 7:1 and the energy profile of Sr2S8G0 is very similar to that of Sr2S0G8. This means that singly doped structures could provide a more accurate estimation of the activation energy from energy profiles than doubly doped structures.

There are some energy profiles that show "overlap"; for different hops of the same final and initial energies, two or more different saddle points may exist (for example, structures Sr2S1G7 and Sr2S7G1 in Figure 6, and Sr2S8G0 in Figure 7). This signifies that the position of the vacancies plays an important role in determining the ionic conductivity.

Figures 8 – 11 compare the trends in the variation of the activation energy as a function of the samarium mole fraction from the computational results obtained in this work with the experimental results in (5).

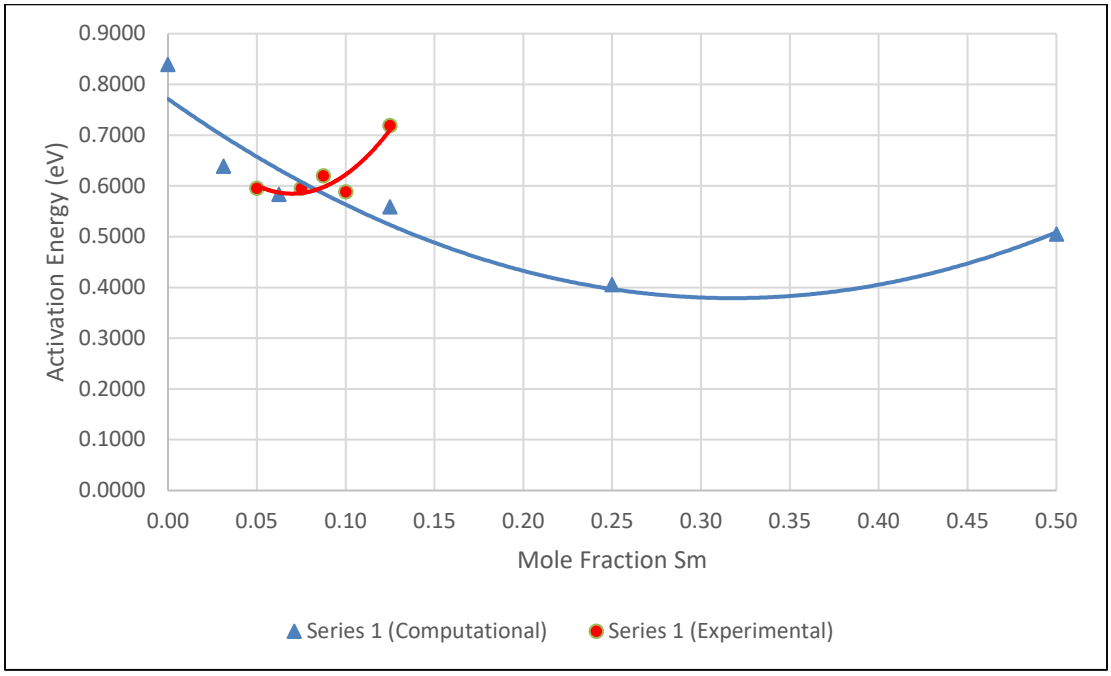

Figure 8. Comparison of the computational and experimental variation of the activation energy with Sm mole fraction for compositional Series 1 and doping strategy DSα.

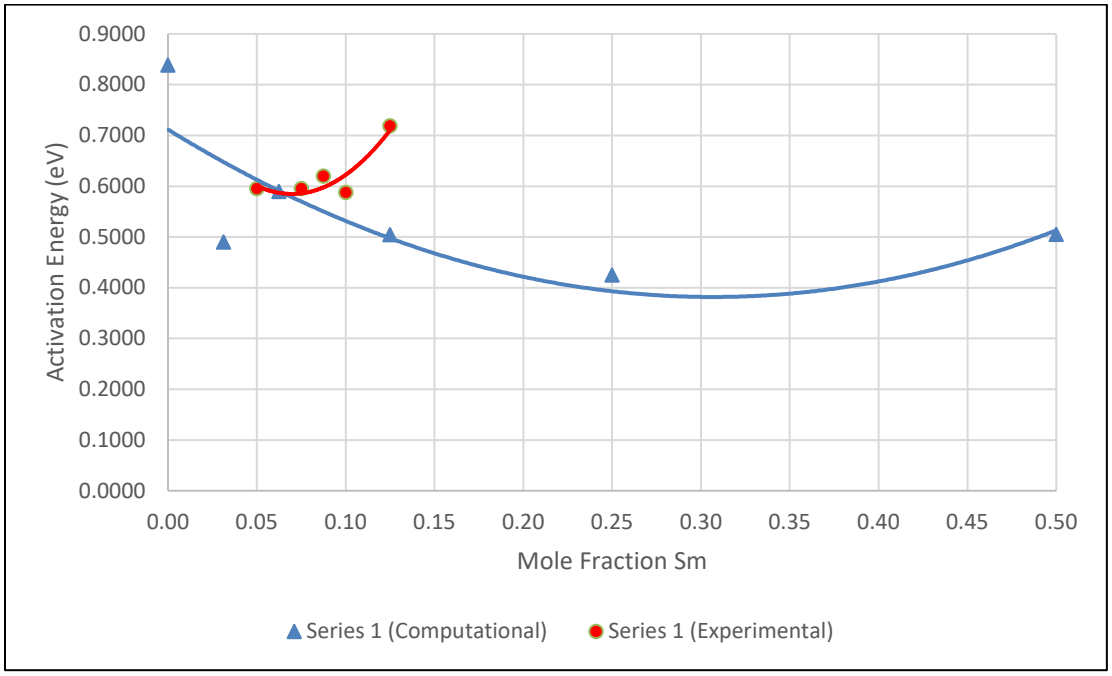

Figure 9. Comparison of the computational and experimental variation of the activation energy with Sm mole fraction for compositional Series 1 and doping strategy DSβ.

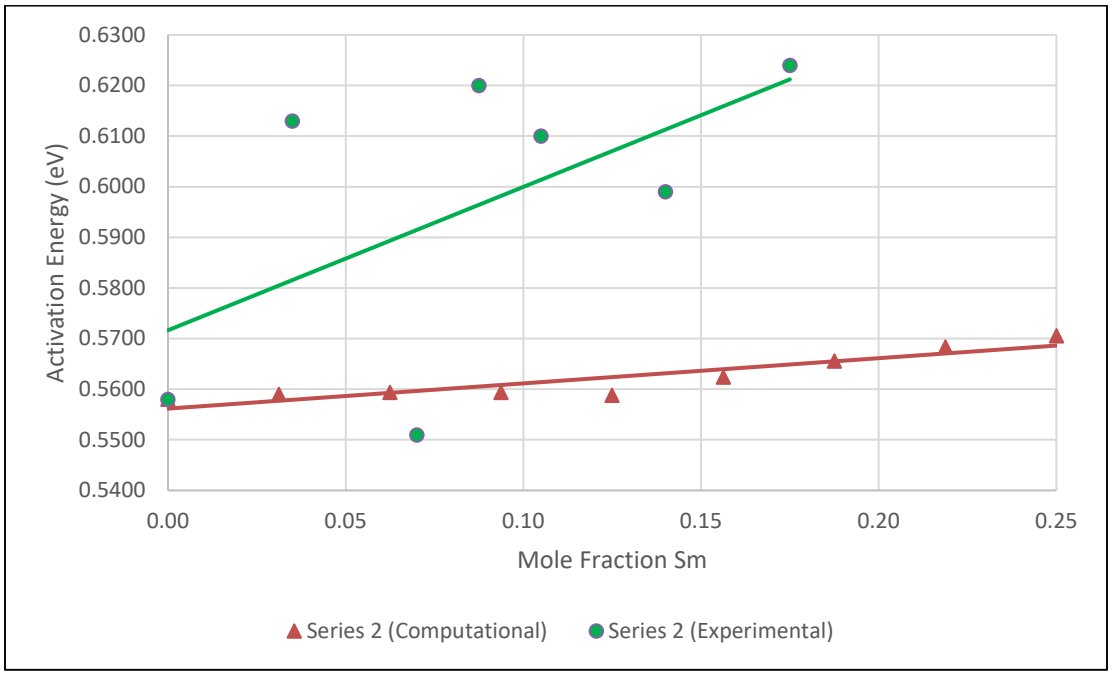

Figure 10. Comparison of the computational and experimental variation of the activation energy with Sm mole fraction for compositional Series 2 and doping strategy DSα.

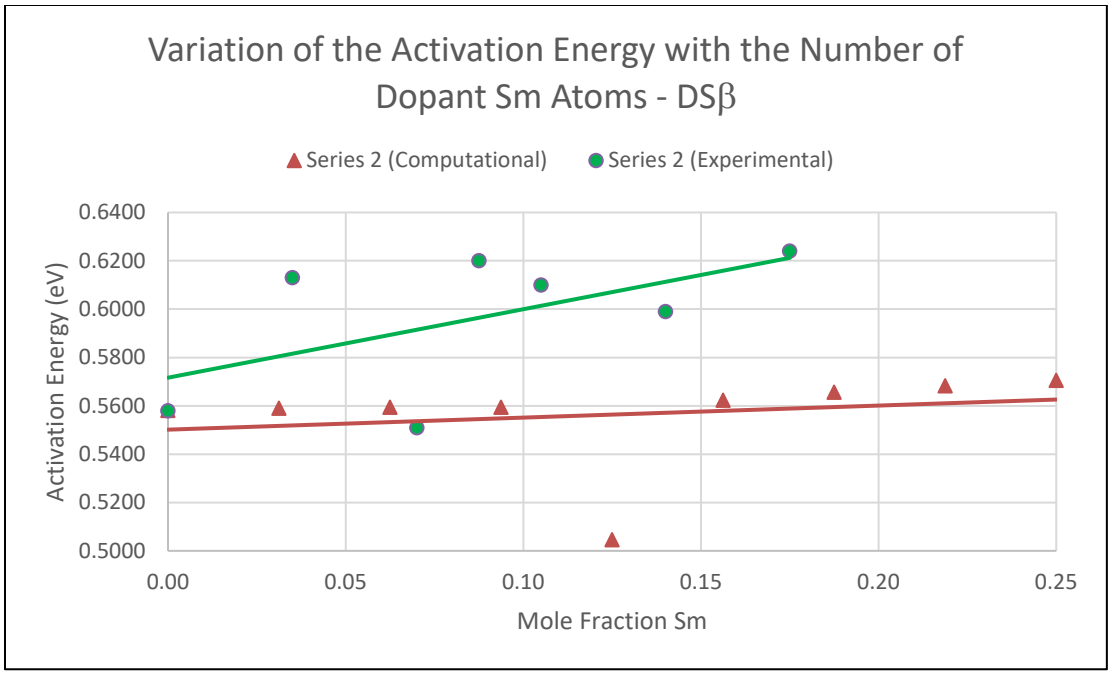

Figure 11. Comparison of the computational and experimental variation of the activation energy with Sm mole fraction for compositional Series 2 and doping strategy DSβ.

The graphical trends of the computational results of the activation energy for Series 1 are similar for DSα and DSβ (Figures 8 and 9) as well as for Series 2 (Figures 10 and 11). The differences in the computational values of the activation energy between DSα and DSβ are nonsignificant ($p > .05$) for both Series 1 and Series 2. This result signifies that the positions of dopants and vacancies within the structures of the same compositional series do not affect the activation energy of a specific structure.

The domain of the computational results of the activation energy for Series 1 is much wider than that of the experimental results (see Figures 8 and 9). Thus, the graphical trends of the computational and experimental results appear to be different, but the statistical analysis of the differences between the computational and the experimental results shows that the differences are nonsignificant ($p > .05$) for both DSα and DSβ structures. This means that the activation energy results obtained computationally are comparable with the experimental results when the doped crystals have equal amounts of dopants. Moreover, it should be noted that the computational results identified a minimum value of activation energy (maximum conductivity) at equal doping mol ratio of Sm and Gd of 0.3; a result that was not obtained experimentally due to the limited dopant mol domain of the experiment.

On the other hand, the graphical trends of the computational and experimental results of the activation energy for Series 2 appear to be similar (see Figures 10 and 11), but the statistical analysis of the differences between the computational and the experimental results shows that the differences are significant ($p < .05$) for both DSα and DSβ structures. There is a discrepancy between computational and experimental activation energy results when the amounts of dopants in a crystal are not equal.

The limitations imposed on the computational procedure of the activation energy, such as limiting the number of images (or replicas) in the NEB calculation to 3 images and utilizing non-random doping profiles may have contributed to mixed results for the activation energy.

Conclusion

The results of the computational simulations are comparable with those obtained experimentally, especially if there are equal amounts of Sm and Gd dopants in the structure. The simulations were able to show that the positions of dopants are crucial in determining the lattice parameter of the doubly-doped crystal if the amounts of the two dopants are unequal, while they play a minor role if the amounts of dopants are equal. Simulation also showed that the positions of vacancies determine the energy barriers to oxide ion migration within the crystal. Computational modelling can contribute to our understanding of the ionic conduction within the electrolyte crystal.

The incongruence of the computational and experimental results can be minimised by avoiding the limitations of the molecular mechanics force field methodology utilised in this study: it is expected that an ab initio density functional theory (DFT) calculation would yield closer conformance. Also, computational results can be improved if the simulation closely models the experimental setup. It is believed that simulation would yield more accurate results for the lattice parameter and the activation energy if the doping strategies were confined to an explicitly random positioning of the dopants inside the crystal. Considering the temperature and the bonding between atoms would improve the lattice parameter results and increasing the number of images in the nudged elastic band (NEB) method would improve the activation energy results.

To improve computational results, the use of computationally intensive procedures will be needed, but with the fast emergence of new technologies that enhance the processing power of parallel computing systems, more rigorous calculations will soon be possible.

Acknowledgments

All calculations were carried out using the Kennedy Supercomputer Infrastructure of the High-Performance Computing (HPC) cluster at the University of St. Andrews.

References

1. D. A. Andersson, S. I. Simak, N. V. Skorodumova, I. A. Abrikosov, and B. Johansson, *Proc. Natl. Acad. Sci.*, **103**, 3518–3521 (2006).
2. S. Omar, E. Wachsman, and J. Nino, *Solid State Ion.*, **177**, 3199–3203 (2006).
3. S. Omar, E. D. Wachsman, J. L. Jones, and J. C. Nino, *J. Am. Ceram. Soc.*, **92**, 2674–2681 (2009).
4. A. V. Coles-Aldridge and R. T. Baker, *Solid State Ion.*, **316**, 9–19 (2018).
5. A. V. Coles-Aldridge and R. T. Baker, *Solid State Ion.*, **347**, 115255 (2020).

6. A. R. West, *Solid State Chemistry and Its Applications*, Second Edition., John Wiley & Sons, Ltd., UK, (2014).
7. J. Hutter, M. Iannuzzi, F. Schiffmann, and J. VandeVondele, *Wiley Interdiscip. Rev. Comput. Mol. Sci.*, **4**, 15–25 (2014).
8. H. Fruchtl, *Cryst*, School of Chemistry, University of St. Andrews, St. Andrews, Scotland, (2019).
9. C. Artini, M. Pani, MM. Carnasciali, MT. Buscaglia, J. R. Plaisier, and G. A. Costa, *Inorg. Chem.*, **54**, 4126–4137 (2015).
10. U. Essmann, L. Perera, M. L. Berkowitz, T. Darden, H. Lee, and L. G. Pedersen, *J. Chem. Phys.*, **103**, 8577–8593 (1995).
11. M. Frigo and S. G. Johnson, *Proc. IEEE*, **93**, 216–231 (2005).
12. G. W. Watson and A. K. Lucid, in *2018 IEEE 18th International Conference on Nanotechnology (IEEE-NANO)*, 1–2, IEEE, Cork, Ireland (2018).
13. O. Alcaraz and J. Trullàs, *J. Mol. Liq.*, **136**, 227–235 (2007).
14. M. Salanne, B. Rotenberg, S. Jahn, R. Vuilleumier, C. Simon, P. A. Madden, *Theor. Chem. Acc.*, **131**, 1143 (2012).
15. A. K. Lucid, A. C. Plunkett, and G. W. Watson, *Johns. Matthey Technol. Rev.*, **63**, 247–254 (2019).
16. K. T. Tang and J. P. Toennies, *J. Chem. Phys.*, **80**, 3726–3741 (1984).
17. U. Kleinekathöfer, K. T. Tang, J. P. Toennies, and C. L. Yiu, *J. Chem. Phys.*, **107**, 9502–9513 (1997).
18. F. Jensen, *Introduction to Computational Chemistry*, 3rd ed., John Wiley & Sons, Ltd., Chichester, UK, (2017).
19. D. A. G. Vieira and A. C. Lisboa, *Eur. J. Oper. Res.*, **235**, 38–46 (2014).
20. G. Pizzi, A. Togo, and B. Kozinsky, *MRS Bull.*, **43**, 696–702 (2018).
21. G. Henkelman, B. P. Uberuaga, and H. Jónsson, *J. Chem. Phys.*, **113**, 9901–9904 (2000).
22. H. Jonsson, G. Mills, and K. W. Jacobsen, in *Classical and Quantum Dynamics in Condensed Phase Simulations*, B. J. Berne, G. Ciccotti, and D. F. Coker, Editors, p. 20, World Scientific, Singapore (1998).
23. M. Mogensen, *Solid State Ion.*, **129**, 63–94 (2000).
24. M. Mogensen, D. Lybye, N. Bonanos, P. Hendriksen, and F. Poulsen, *Solid State Ion.*, **174**, 279–286 (2004).